On the role of cationic defects over the surface reactivity of manganite-based perovskites for low temperature catalytic oxidation of formaldehyde

Yin Xu, Jeremy Dhainaut, Jean-Philippe Dacquin, Jean-Francois Lamonier, Hui Zhang, Sebastien Royer

On the role of cationic defects over the surface reactivity of manganite-based perovskites for low temperature catalytic oxidation of formaldehyde

Yin Xu,[a,b,c] Jérémy Dhainaut,[b,*] Jean-Philippe Dacquin,[b] Jean-François Lamonier,[b] Hui Zhang,[a,*] Sébastien Royer[b]

[a] Department of Environmental Science and Engineering, Hubei Environmental Remediation Material Engineering Technology Research Center, Wuhan University, Wuhan 430079, China

[b] Univ. Lille, CNRS, Centrale Lille, Univ. Artois, UMR 8181-UCCS-Unité de Catalyse et Chimie du Solide, F-59000 Lille, France

[c] Hubei Key Laboratory of Regional Development and Environmental Response, Faculty of Resources and Environmental Science, Hubei University, Wuhan 430062, China

[*]Corresponding Authors: jeremy.dhainaut@univ-lille.fr (J. Dhainaut)

eeng@whu.edu.cn (H. Zhang)

Abstract:

Defect engineering in catalytic materials is a versatile strategy to fine-tune their performance towards oxidation reactions, and break the related bottlenecks. Herein, a series of $La_{1-x}MnO_3$ perovskite-based materials was designedly synthesized to investigate the effect of cation defects on their physico-chemical properties. Based on extensive characterizations and density function theory (DFT) calculations, it is demonstrated that La-deficiency could orderly induce oxygen vacancies and electronic structure regulation on perovskite, which prominently promotes the catalytic activity towards formaldehyde oxidation. The leading material ($La_{0.6}MnO_3$) could retain high activity for 63 hours, either under dry or humid air. In brief, this work unveils the feasibility of modulating the surface reactivity by modifying the electronic structure properties of lanthanum manganite perovskites following simple adjustment of the A-site cationic vacancies, and also highlights A-site deficient perovskite as a potentially efficient catalyst for environmental remediation.

Keywords: Perovskite; Lanthanum deficiency; Surface defects; Electronic structure regulation; Formaldehyde oxidation

1. Introduction

Perovskites might represent the most studied mixed-oxide structures, owing to their exceptional thermal stability, ionic conductivity, electronic structure, electron mobility, and redox behavior [1,2]. Perovskite structures can be expressed with a general formula ABO_3, where the A-site cation is 12-fold coordinated with oxygen, while the B-site cation is 6-fold coordinated with oxygen [2]. As a benefit of a wide range of possible substitutions at both A and B sites, perovskites offer great flexibility allowing to tailor their physicochemical properties and better target specific applications. The B-site cations were found to play a primary role in altering the electronic structure of the perovskites, thus modifying the catalytic efficiency [1-3]. In particular, manganese-based perovskites are emphasized as possible alternatives for noble metal-based catalysts (Pt, Rh, Pd), mainly due to their relatively low cost, good thermal stability at high temperature and ease of preparation [4]. For instance, lanthanum manganite perovskites (A = La; B = Mn) provide redox (Mn^{4+}/Mn^{3+}) active centers to facilitate a wide variety of catalytic reactions [1,5,6].

The catalytic activity of perovskites can be modulated by altering their crystallinity, morphology, microstructure or surface/interface chemical states. Different strategies were hence developed to improve the performance of stoichiometric perovskites, such as increasing the specific surface area, doping with transition metals or other lanthanides and rare earths, or modifying the crystal structures and morphologies [3,7]. Among these, doping is the most common and efficient strategy. For example, aliovalent substitutions on A- or B-sites using cations of different valences, like K^+, Sr^{2+} or Ce^{4+}, were reported [5,8]. To meet the criteria of electron neutrality, this substitution was suggested to either change the oxidation state of the transition metal cation (in B-position) or introduce oxygen vacancies, facilitating oxygen transfer and thus

increasing oxygen mobility.

As a kind of surface defects, oxygen vacancies have been widely reported to act as adsorption and active sites in heterogeneous catalytic reactions. However, cation vacancies are another kind of important defects, which have been often overlooked. For instance, as-prepared MnO_2 often tends to exhibit Mn vacancies (with 2.8 ~ 11.1 mol%) [9], and these vacancies can significantly change the electronic structure and photoconductivity of the material [10]. Recently, cation vacancies have been also generated to promote the catalytic activity of perovskites in oxygen evolution reactions (OER) [11-13]. For instance, a cation deficiency-promoted phase separation strategy was applied to prepare perovskite-based composites with significantly enhanced H_2O oxidation performances owing to improved mobility of lattice oxygens as ionic oxygen species [11]. The SnCoFe perovskite hydroxide ($SnCo_{0.9}Fe_{0.1}(OH)_6$) with Sn cation deficiency exhibited excellent OER activity due to the promoted exposure of active CoFe sites and improved conductivity [14]. A-site deficiency in La-Ni and La-Fe perovskites also led to an enhanced OER activity, which has been attributed to the generated surface oxygen vacancies and improved metal-oxygen hybridization [15,16]. Thus, cationic defects modulation in perovskite oxides is an effective strategy to modify their physical and chemical properties which should be further studied and applied to VOCs oxidation reactions.

While most of the research effort focused on stoichiometric lanthanum manganite perovskites with varying oxygen excess, commonly noted $LaMnO_{3+\delta}$, it should be noted that those structures are actually defective in both La and Mn positions [17]. Thus, a more rigorous formula would be $La_{1-x}Mn_{1-x}O_3$. For instance, a δ value of 0.158 corresponds to ~5 % of La and Mn vacancies ($La_{0.95}Mn_{0.95}O_3$), though the La/Mn vacancy ratio can also be controversial [18,19]. In particular, a deficiency of A-site ions

in the perovskite lattice ($A_{1-x}B_{1-y}O_3$, with x > y) leads to self- (or vacancy-) doped perovskites [20]. The latter materials showed intriguing results in heterogeneous catalysis and especially in oxidation reactions [21,22].

Formaldehyde (HCHO), as one of the dominating indoor air pollutants, is mainly emitted from various building materials and household products [23]. Long term exposure to HCHO may cause irritation of the eyes and of mucosa of the upper respiratory tract. In 2004, the International Agency for Research on Cancer (IARC) classified HCHO as carcinogenic for humans (Group 1) [24]. Various conventional approaches such as adsorption, plasma technology, photocatalytic oxidation, and thermal catalytic oxidation have been applied for the removal of HCHO [25,26]. Among them, mild temperature catalytic oxidation (< 100 °C) is considered as an attractive technology for HCHO abatement. It overcomes the disadvantages of relatively short adsorbents lifetime, additional apparatus and operating costs of plasma technology and photocatalytic oxidation.

Currently, noble metal-based catalysts (*i.e.* Pt, Pd, Rh, Au and Ag-doped materials) present the highest catalytic activities in HCHO oxidation [27,28]. However, their high cost limits real-life applications, and transition metal oxide-based catalysts would be preferred [29-32]. In particular MnO_x-based materials are under extensive investigation, as they show the best catalytic activity among transition metal oxides. Surprisingly, Mn-based perovskites have been scarcely reported for HCHO oxidation though they have been applied to a wide range of volatile organic compounds (VOCs) [5,33]. In this work, a series of lanthanum manganite perovskite-based materials was prepared. The molar concentration of lanthanum was modulated during the synthesis, resulting in materials having $La_{1-x}MnO_3$ as a general formula (with x = 0, 0.1, 0.2, 0.3 and 0.4). This series was extensively characterized and tested for the mild oxidation of HCHO.

By combining extensive characterization, density function theory (DFT) calculations, and catalytic results, better understanding of the influence of cationic vacancies on the catalytic performances of perovskite-based materials is provided herein.

2. Experimental

2.1. Synthesis of catalysts

A series of manganese-based $La_{1-x}MnO_3$ perovskite materials (with x = 0, 0.1, 0.2, 0.3 and 0.4) was prepared following the citrate complexation method described in more details in a previous work [34]. Briefly, the $La_{1-x}MnO_3$ catalysts were prepared starting from the following molar ratio of reagents: (1-x) $La(NO_3)_3 \cdot 6H_2O$ (≥ 99.0 %, Sigma-Aldrich) : 1 $Mn(NO_3)_2 \cdot 4H_2O$ (97.0 %, Aldrich) : (2-x) $C_6H_8O_7$ (+99.5 %, Alfa Aesar). All reagents were dissolved in distilled water, and the resulting homogeneous solutions were kept under stirring at room temperature overnight. Excess water was eliminated by rotary evaporation, resulting in gels which were further thermally treated under air over two steps: 180 °C for 1 h (3 °C min^{-1}), and 700 °C for 8 h (2 °C min^{-1}) excepted in the case of $La_{0.7}MnO_3$ and $La_{0.6}MnO_3$, for which the second temperature step was adjusted at 750 °C to obtain fully crystalline perovskite phases. The reason will be discussed in section 3.1. The reference Mn_3O_4 was prepared in the same way, with no addition of lanthanum nitrate (x = 1). The gel was thermally treated at 1000 °C for 4 h (2 °C min^{-1}) [19].

2.2 HCHO catalytic oxidation

Formaldehyde (HCHO) oxidation was performed in a fixed bed reactor (internal diameter = 8 mm), loaded with 0.20 g of the catalyst. Catalyst activation was performed *in situ* at 300 °C for 1 h under 20 vol% O_2/He, with a flow rate of 100 mL·min^{-1}. Gaseous formaldehyde was produced from paraformaldehyde in a permeation tube placed in a permeation chamber (Dynacalibrator, VICI Metronics, Inc.) and kept at

100 °C. The reacting gas containing 100 ppm of HCHO in 20 vol% O_2/He was flowed through the fixed bed reactor and its temperature was controlled by applying a temperature decrease rate of 0.5 °C min^{-1} from 300 to 100 °C, and of 0.2 °C min^{-1} from 100 to 25 °C. The total flow rate was 100 mL min^{-1}, corresponding to a gas hourly space velocity (GHSV) of 30 L g_{cat}^{-1} h^{-1}. The effluent gas was monitored online by a gas chromatograph (GC, Varian) equipped with a thermal conductivity detector. Separations were performed using two columns: one CP-Sil 5 CB column channel (8 m) for HCHO analysis, and one COX column channel (1 m) for CO_2 analysis.

The HCHO oxidation into CO_2 was expressed as HCHO conversion, while HCHO elimination refers to the removal efficiency of HCHO. They were calculated using the following equations, respectively:

$$\text{HCHO conversion (into } CO_2) = \frac{[CO_2]_t}{[HCHO]_0} \quad (1)$$

$$\text{HCHO elimination} = \frac{[HCHO]_0 - [HCHO]_t}{[HCHO]_0} \quad (2)$$

where $[HCHO]_t$ and $[CO_2]_t$ are their concentration at time *t* as monitored by GC, and $[HCHO]_0$ is the initial HCHO concentration (100 ppm).

During the stability test, a fresh catalyst was first activated as indicated before (300 °C, 1 h under 20 vol% O_2/He, 100 mL min^{-1}). Then the reacting gas (100 ppm HCHO in 20 vol% O_2/He, 100 mL min^{-1}) was passed through the catalyst bed at T_{50} reaction temperature (corresponding to 50 % HCHO conversion) for 63 h.

2.3 Characterization

X-ray diffraction patterns (XRD) were collected on a Bruker D8 Advanced AXS diffractometer equipped with Cu $K_{\alpha 1}$ monochromatic radiation source (λ = 1.5418 Å) and operated at 40 kV and 30 mA. X-ray diffractograms in the 10°-80° region were recorded with a 0.02° step size (step time = 1 s). Scherrer equation ($d = K\lambda/(\beta\cos\theta)$) was performed at an identified diffraction peak which does not overlap with crystalline

impurities, where d is the mean crystallite size (nm), K is a dimensionless shape factor (0.9), λ is the X-ray wavelength (0.15418 nm), β is the full width at half maximum (FWHM, in radians), and θ is the Bragg angle (in radians). Following the thermal treatment of the material series at 1000 °C, their powder diffraction patterns were measured (2θ scan = 10-90 °, 2θ step size = 0.03, integration time = 3 s/step) and analyzed by Rietveld refinement using the Jana2006 freeware. As the starting model, we used a reference structure with a similar chemical composition, $La_{0.945}Mn_{0.945}O_3$ (COD database, card number 1531526). In the structure refinement, cell parameters, sample shift, thermal parameters, and lanthanum and oxygen sites occupancies were considered variable parameters. A Pseudo-Voigt shape function was used to fit the peak shape. *In situ* XRD experiments were performed by first depositing the samples on a kanthal sample holder and XRD patterns were collected every 50 °C from room temperature to 1123 °C, under a gas mixture composed of 3% H_2 diluted in He (50 mL min^{-1}) and after 30 min of sample stabilization at the desired temperature. After recording the XRD pattern at 1123 °C, the sample was cooled down to 30 °C for a last diffractogram recording.

The electron paramagnetic resonance (EPR) spectra were measured on a Bruker (MiniScope MS 5000) spectrometer with a center field of 350 mT, a microwave power of 0.1 mW and a microwave frequency of 9.48 GHz.

Nitrogen sorption measurements were performed at -196 °C on a Micromeritics TriStar II Plus apparatus. Samples were degassed at 150 °C during 6 h prior analysis. Specific surface areas (S_{BET}) were calculated according to the Brunauer-Emmett-Teller (BET) method.

Morphological properties and elemental mapping of the samples were evaluated on a field-emission scanning electron microscope (SEM-FEG Hitachi SU-70) with an energy dispersive spectrometer (EDS) microanalysis (EDAX Genesis).

X-ray Photoelectron Spectroscopy (XPS) was performed on a AXIS Ultra^{DLD} spectrometer (Kratos Analytical) with a monochromatic Al Kα X-ray source (1486.6 eV). High resolution spectra were collected with a constant pass energy (PE = 20 eV) and the binding energy (BE) was calibrated with the adventitious carbon (BE(C1s) = 284.8 eV). Quantification and spectral decomposition were processed using CasaXPS software.

Time-of-flight secondary ion mass spectrometry (ToF-SIMS) analyses were performed on a TOF.SIMS 5 spectrometer (ION TOF GmbH) equipped with a pulsed bismuth liquid metal ion gun as source of primary ions. Bi_3^+ clusters (25 keV, 0.3 pA current) were used to improve molecular information in the spectra. The analyzed sample area was 500×500 μm^2 for spectral analyses with 128x128 pixels and 150 scans.

Temperature programmed reductions (TPR) were carried out on about 60 mg of unpretreated sample under 5 vol% H_2/Ar gas flow (50 mL min^{-1}) with a heating rate of 10 °C min^{-1} up to 1000 °C using a Micromeritics Autochem II 2920 apparatus. The same apparatus was used for O_2 temperature-programmed desorption experiments (TPD) and coupled with mass spectrometry. The catalysts (50 mg) were *in situ* pre-activated under 5 vol% O_2 diluted in He and submitted to the following conditions: 30 mL/min He, temperature from 40 °C to 1000 °C with a ramp of 10 °C/min. The outlet gases O_2 (m/z = 32) were identified using a mass spectrometer. The amount of O_2 desorbed from the catalyst was quantified from calibrated pulses (1 μmol).

Stoichiometry of La and Mn in the solids were monitored by inductively coupled plasma-optical emission spectroscopy (ICP-OES) (Agilent Technologies 700 Series

spectrometer). Before analysis, the solids were dissolved in a concentrated HCl/HNO_3 mixture.

The DFT calculations were carried out using the Vienna Ab-initio Simulation Package (VASP) with the frozen-core all-electron projector-augment-wave (PAW) method. The Perdew-Burke-Ernzerhof (PBE) of generalized gradient approximation (GGA) was adopted to describe the exchange and correlation potential. The cutoff energy for the plane-wave basis set was set to 450 eV. The 2×1 $LaMnO_3$ (001) slab has 2-layers atoms, and a vacuum region of 15 Å above them was used to ensure the decoupling between neighboring systems. For the geometry optimization, the atoms in the bottom layer of slab were fixed to their bulk positions. The geometry optimizations were performed until the forces on each ion was reduced below 0.01 eV/Å, and the Monkhorst-Pack k-point sampling was set to 1×3×1. The resulting structures were then used to calculate the electronic structures, and the k-point sampling was increased to 3×5×1. The formation energies of O-vacancy were calculated by the following formula: E_{form} = E(vacancy) - E(pure) + $\mu(O)$; where E(vacancy) and E(pure) are the total energies of O-vacancy and pure $LaMnO_3$(001), respectively. $\mu(O)$ is the chemical potential of atomic O.

3 Results and Discussion

3.1 Crystal phase structure

XRD patterns of as-synthesized samples are shown in Figure S1. The first three samples ($LaMnO_3$, $La_{0.9}MnO_3$, $La_{0.8}MnO_3$) present the typical diffraction pattern of lanthanum manganite perovskite (JCPDS 50-0298) with characteristic peaks at 2θ = 23.0°, 32.5°, 40.1°, 46.9°, 58.1°, 68.6° and 77.8°. However, the diffractograms of $La_{0.7}MnO_3$ and $La_{0.6}MnO_3$ annealed at 700 °C display a broad hump around 29°, attributed to the presence of an amorphous phase (Figure S2, insert). This hump

disappears following calcination at 750 °C (Figure S1). As reported in the literature [19,35,36], manganese oxide phases MnO_x usually form in lanthanum-deficient perovskites. In order to verify this point, $La_{0.6}MnO_3$ was further calcined at 1000 °C during 4 h and the related XRD pattern is given in Figure S2. A secondary crystalline phase, Mn_3O_4, is unambiguously observed, verifying the presence of amorphous manganese oxide (Mn_xO_y) phase at 700 °C. To obtain more detailed analysis of their crystalline composition, all samples were thermally treated at 1000 °C and the related XRD patterns are given in Figure S3. Following the semi-quantitative analysis of their crystalline composition, it appears that all solids contain La_2O_3, $La(OH)_3$, and Mn_3O_4 in various proportions, with more Mn_3O_4 formed following further La-deficiency as indicated in Table S1. Furthermore, Rietveld refinement was performed on these XRD patterns (Figure S3) and the calculated lattice parameters are given in Table S1. It appears that all perovskites present a similar composition La_xMnO_3 with a slight deficiency in lanthanum (x = 0.89-0.92), as shown by Gao et al [37]. Thus, it can be concluded that all catalysts thermally treated at 700-750 °C are actually composed of La_xMnO_3 perovskite (x = 0.9 ± 0.02) decorated with amorphous $La_xO_y(OH)_z$ and Mn_xO_y species. The presence of the latter have a great influence over the surface redox properties of the perovskites as determined hereafter.

As seen in Table 1, the crystallite size of the samples decreased from 26 to 19 nm with the decrease of the La/Mn ratio, when applying the Scherrer equation to the (024) plane (2θ = 46.9°) [34]. The textural properties are also presented in Table 1. As expected for perovskite materials, all catalysts have relatively low specific surface areas (from 18 to 24 $m^2\ g^{-1}$) due to high temperature calcination and lack of significant internal porosity in the aggregates. The surface morphology of $La_{0.6}MnO_3$ was visualized by FEG-SEM. As shown in Figure S4, this sample is composed of

agglomerated small particles with an irregular morphology and forming large macropores, which is very similar to reference $LaMnO_3$ perovskite [34]. EDS mapping of the sample further shows that La, Mn and O elements are homogeneously distributed on the surface (Figure 1), while EDS spectra allow to evaluate the La/Mn atomic ratio to be 0.50 instead of 0.60 (Figure S5), which could be attributed to the presence of extra-framework Mn species. Moreover, the O/Mn atomic ratio is found be 2.32, much lower than the expected stoichiometry for a reference perovskite and supporting the presence of single oxide species (MnO or $Mn3O_4$) at the surface.

3.2 ICP and XPS analysis

To go further in details on the elemental composition and chemical states, bulk (ICP-OES) and surface (XPS) analyses were conducted and the related quantitative elemental compositions including La/Mn, Mn/O and La/O atomic ratios are summarized in Table 2. The XPS spectra for La 3d and Mn 2p, and Mn 3s and O 1s core levels are given in Figures S6 and 2, respectively. Within experimental and apparatus errors, the determined atomic ratios of La/Mn by ICP follow closely the La/Mn ratios in the initial solutions. According to XPS, a slight deficiency of La ($La_{0.9}MnO_3$ and $La_{0.8}MnO_3$) in the perovskite structure induces a strong decrease of both La/O (from 1.06:3 to 0.52:3) and Mn/O (from 0.95:3 to 0.71:3) surface atomic ratios, suggesting that La-deficiency resulted in the formation of both La and Mn cationic vacancies (V_{La} and V_{Mn}) at the surface. Further La-deficiency ($La_{0.7}MnO_3$ and $La_{0.6}MnO_3$) does not further change significantly the La/O surface atomic ratio (0.56:3 to 0.51:3), however the Mn/O surface atomic ratio dramatically increases from 0.71:3 to 1.21:3. Moreover, La/Mn atomic ratios as determined by XPS are systematically lower than by ICP for La-deficient perovskites, all pointing to surface enrichment in manganese as framework cations and extra-framework oxides.

High-resolution Mn 3s XPS spectra can be observed in Figure 2a. The average oxidation state (AOS) of the surface Mn was determined by the binding energies of the doublet separation of Mn 3s ($\triangle E_s$) following the correlation: AOS (Mn) = 8.956 – 1.126 × $\triangle E_s$ [38]. For the stoichiometric $LaMnO_3$, the AOS (Mn) is about 3.42 (Table 2), in agreement with a mixture of $Mn^{4+/3+}$ with Mn^{3+} as the predominant cation. $La_{0.9}MnO_3$ and $La_{0.8}MnO_3$ present similar AOS (Mn) of 3.40 and 3.41, respectively. Further La-deficiency led to a more marked decrease of the AOS (Mn) towards 3.36 and 3.33 for $La_{0.7}MnO_3$ and $La_{0.6}MnO_3$, respectively. Assuming constant AOS (Mn) of perovskite, this confirms the presence of Mn-oxide phase with Mn valency ≤ 3 for these last two samples.

Figure 2b displays the XPS spectra in the O1s region for all samples. Three peaks can be observed around 529.3, 531.1, and 532.8 eV, representing the surface lattice oxygen (O^{2-}, denoted as O_{latt}), the surface adsorbed oxygen species (such as O_2^{2-} or O^- belonging to defect-oxides and OH groups, denoted O_{ads}), and molecular water adsorbed on the surface (denoted O_w), respectively [34].

Table 2 also presents the proportion of the different oxygen species. The fraction of surface adsorbed oxygen species initially increases slightly with the deficiency in lanthanum. These O_{ads} species are usually linked to surface oxygen vacancies (V_O) [39], the former being highly mobile, while the latter provides sites for adsorption, activation and migration of oxygen species. Further La-deficiency leads to a marked decrease of O_{ads} fraction, along with an increase in the fraction of surface lattice oxygen O_{latt}. Some previous works reported that O_{ads} plays a major role in the oxidation of HCHO [30,40], while others pointed out that O_{latt} is mainly responsible for the catalytic activity in HCHO oxidation [29,41]. Most likely, both oxygen species can play a key role in oxidation reactions, depending on the reaction conditions leading to either a suprafacial

or an intrafacial oxidation mechanism.

3.3 Defects analysis and theoretical calculations

In order to estimate the content of anionic vacancies in the different materials, solid-state EPR and Raman spectra were obtained to complete XPS analysis. As seen in Figure 3, all samples exhibit a signal at a g-value of 2.002, which is attributed to unpaired electrons trapped by the oxygen vacancies. Most surprisingly, the EPR signal of the $La_{1-x}MnO_3$ samples linearly increases with increasing the deficiency of La up to x = 0.3 (Figure 3, insert), implying that the amount of oxygen vacancies on the catalyst could be precisely modulated by simply adjusting the ratio of A site : B site cations. However, it should be noted that further deficiency in A-site cations ($La_{0.6}MnO_3$) causes a drastic decrease in the amount of oxygen vacancies. This might indicate that, if the amount of oxygen vacancies exceeds a threshold value, the structure would partially collapse with the formation of a new external phase (*i.e.* Mn_xO_y) in addition to the perovskite phase.

The existence of defects is further confirmed by Raman spectroscopy (Figure S7). Raman bands around 490 and 610 cm^{-1}, respectively associated to bending- and stretching-like vibrations of the MnO_6 octahedra [42], might reflect the extension and compression of Mn-O bond pairs, correlated with Jahn-Teller distortion [42,43]. As observed, the large band from 300 to 700 cm^{-1} in $La_{0.8}MnO_3$ is more intense and broader than the dual bands in $LaMnO_3$ centered at 490 and 610 cm^{-1}. This indicates higher distortion of MnO_6 octahedra by the Jahn–Teller effect and consequently, the presence of more oxygen vacancies [44]. These results are consistent with EPR spectra. As expected, the reduction of lattice oxygen results in the generation of coordinatively unsaturated metal centers, as well as lattice dislocation and disordered local structure, all leading to electrostatic repulsion between positively charged oxygen vacancies and

Mn^{3+} cations, and the subsequent lattice distortion/expansion. Of note, $La_{0.6}MnO_3$ spectrum does not show a similar large band, in line with EPR observations showing the presence of few oxygen vacancies. In contrast, a new band at 642 cm^{-1} appears, assigned to Mn–O stretching mode of Mn_xO_y species [45]. Importantly, this redshift corresponds to a weakening of Mn-O bonds [46], and thus higher lattice oxygen activity in line with the increase of O_{latt}/O_{tot} observed by XPS.

To understand the origin of oxygen defects and their role in the catalytic activity enhancement of La-deficient perovskites, density function theory (DFT) calculations were performed to study the oxygen vacancy formation energy (E_{OV}) and the density of states (DOS), respectively. A $LaMnO_3$ crystal with Mn-terminated (001) surface was chosen as our calculation model, due to the facts that it is the most stable surface, and the redox active Mn atoms are expected to be the main active sites for catalytic oxidation [47].

Models of stoichiometric and La-deficient ($La_{1-x}MnO_3$, with x slightly inferior to 0.1) perovskite surfaces, with and without oxygen vacancy, are shown in Figure 4. Based on energy minimization, the E_{OV} of a perfect $LaMnO_3$ plane is 3.203 eV, which is higher than that of a $La_{1-x}MnO_3$ plane (2.724 eV). Lower E_{OV} evidences that La-deficiency effectively promotes the formation of oxygen vacancies, confirming the result of solid EPR experiments. In addition, the length of two Mn-O bonds (I_{Mn-O1}, I_{Mn-O2}) were further calculated in the stoichiometric $LaMnO_3$ (Figure 4a) and in the La-deficient $La_{1-x}MnO_3$ with oxygen vacancy (Figure 4d). Interestingly, I_{Mn-O1} and I_{Mn-O2} are significantly extended from 1.837 and 1.987 to 2.002 and 2.043 Å, respectively, by introducing La and O vacancies. The stretched Mn-O bonds should result in higher lattice oxygen reactivity.

As mentioned above, it is assumed that introducing La defects into $LaMnO_3$ would

lead to partial reduction of Mn^{4+} to Mn^{3+}. That is, unpaired electrons would fill empty e_g orbitals to move from the $t_{2g}^3e_g^0$ to the $t_{2g}^3e_g^1$ electronic configurations. Such e_g orbital occupation can cause a spin hole in oxygen via exchange interactions [48]. Consequently, the e_g electrons would become delocalized and produce a spin channel connecting the Mn cations to the O anions, further creating an unimpeded spin route to accelerate charge transfers and thus redox reactions.

To support this viewpoint, the DOS patterns, which are intuitive evidence of the variation of electronic structure, were simulated *via* DFT. As observed in Figure 5a-b, the *d*-band center of Mn 3d is calculated at -1.434 and -1.382 eV for $LaMnO_3$ and $La_{1-x}MnO_3$, respectively. Hence, in the presence of La vacancy, the *d*-band center shifted towards Fermi level (E_F) as a result of the increase of antibonding states [49]. It is considered that antibonding electrons with high energy are unstable, thus resulting in e_g orbital electrons being more active for redox reactions. Similarly, as illustrated in Figure 5c-d, the *p*-band center of O 2p also shifted towards E_F level: from -3.938 to -3.824 eV for $LaMnO_3$ and $La_{1-x}MnO_3$, respectively. This can be interpreted as the lattice oxygen becoming more favorable thermodynamically to participate in redox mechanism. Both Mn 3d and O 2p state shifts indicate that charge transfers between Mn and O-related adsorbates (*i.e.* O^{2-} and O_2^{2-}) would accelerate in La-deficient $La_{0.9}$ perovskites, facilitating the oxidation of Mn species.

Based on these observations, it is assumed that the electronic structure of Mn-O bands can be modulated by introducing La vacancies, which would affect the catalytic activity of perovskites in redox reactions.

3.4 Low temperature redox studies

The H_2-TPR tests were performed to investigate the reducibility of the series of catalysts and related data are shown in Figure 6 and Table 3, respectively. For $LaMnO_3$,

the main peak is centered at 371 °C, with a shoulder at 448 °C which can be assigned to the reduction of Mn^{4+} into Mn^{3+} as well as a part of Mn^{3+} ions into Mn^{2+}, respectively. From 600 °C, an additional intense peak corresponds to the reduction of the remaining Mn^{3+} to Mn^{2+}. The calculated total H_2 consumption is 2.66 mmol/g, fitting with the total reduction of Mn ions (Mn^{3+} and Mn^{4+}) constituting a stoichiometric $LaMnO_{3.15}$ perovskite into Mn^{2+}.

The main peak for the three less La-deficient perovskites ($La_{0.9}MnO_3$ to $La_{0.7}MnO_3$) is centered on a similar temperature from 370 °C to 379 °C. In contrast, the main peak for $La_{0.6}MnO_3$ is shifted towards higher temperature (395 °C), which can be attributed to the presence of manganese oxide [50]. A small shoulder (Figure 6, area highlighted in yellow) is observed at low temperature (~ 255 °C) for all samples. It is most likely due to the removal of surface reactive oxygen species. The corresponding initial H_2 consumption rates of the first reduction shoulder (before occurrence of phase transformation) have been calculated, and the results are indicated in Figure S8. This rate increases with decreasing the La/Mn ratio and indicates that partial deficiency in A-site (La^{3+}) cations, along with the formation of Mn_3O_4 species from $La_{0.7}MnO_3$, promote the low temperature reducibility of the $LaMnO_3$-based catalysts, probably through increasing the concentration of surface oxygen reactive species (such as O_2^{2-}, O^-, and OH groups), with expected beneficial influence over HCHO oxidation.

To get more insights into the reduction mechanism, *in-situ* temperature-controlled XRD under H_2 flow was conducted on $La_{0.6}MnO_3$ to evidence the progressive Mn^{4+} reduction process. XRD patterns in the range of 25 to 800 °C are shown in Figure 7. Small peaks attributed to La_2O_3 and MnO are observed from 25 °C under reducing conditions. Such a low temperature further reveals the presence of surface reactive species including $La_xO_y(OH)_z$ and Mn_xO_y, knowing that the latter can be reduced into

MnO at low temperature [50]. Furthermore, the diffraction peaks attributed to the $LaMnO_3$ crystalline phase started to decrease in intensity from 200 °C, confirming the facilitated reduction of Mn^{4+} composing the perovskite phase in this A-deficient composition. On the other hand, the intensities of La_2O_3 and MnO reflections gradually increase with increasing the temperature of reduction. From 600 °C under reductive conditions, the perovskite phase almost disappears from the XRD patterns, indicating its complete reduction which correlate well with TPR results (Figure 6).

O_2-TPD tests were carried out to estimate both the surface and bulk oxygens reactivity. As indicated in Figure S9, three regions (III, II, I) respectively refer to the release of bulk lattice oxygen (O_{latt}, above 750 °C); the desorption of β oxygen species (β-O_2, at T = 440 − 750 °C) attributed to the reduction of bulk Mn(IV) species by the outward diffusion of oxygen species; and α oxygen species including weakly adsorbed surface oxygen species and some active oxygen species from the subsurface lattice (O_2^-) (α-O_2, at T = 100 − 440 °C). Strikingly, compared with $LaMnO_3$ and $La_{0.8}MnO_3$, $La_{0.6}MnO_3$ has more surface active oxygen species and especially more easily-released lattice oxygen species (0.21 and 0.41 versus 0.88 mmol of desorbed O_2 per gram, respectively). In line with the above discussion, their increased concentration is directly related to the presence of abundant amorphous Mn_xO_y species. These weakly bonded oxygen atoms are expected to participate in oxidation reactions.

3.5 Catalytic activity

The catalysts performance towards formaldehyde (HCHO) oxidation into CO_2 is shown in Figure 8a, and the related data are given in Table 4. In line with the observations made, the conversion efficiency increases with increasing the La-deficiency, even with the presence of Mn_3O_4 species on the surface of $La_{0.7}MnO_3$ and $La_{0.6}MnO_3$. The T50 (defined as the temperature needed to convers 50 % of HCHO into

CO_2) is lowered from 145 °C ($LaMnO_3$) to 128 °C with the best catalyst of this series, $La_{0.6}MnO_3$. Mn_3O_4 (which may not be the manganese oxide present at the surface of the perovskites at 750 °C) itself is poorly active, as seen on Figure S10, with a T_{50} of 205 °C. The apparent activation energies (E_a) were also calculated from the Arrhenius plots given on Figure 8b. E_a decreases from 96.4 kJ/mol ($LaMnO_3$) to 43.7 kJ/mol ($La_{0.6}MnO_3$), within the range of A-site substituted perovskites [33] and most supported noble metal catalysts [51,52].

Based on the characterization conducted, this catalytic improvement can be attributed to the cumulated effect of several factors: Figure S11 shows the linear decrease of E_a with decreasing the La/Mn ratio (in the bulk and on the surface) and the Mn average valence. Additionally, more oxygen vacancies (O_{vac}) should decrease E_a to some extent, as discussed. However, herein $La_{0.6}MnO_3$ both presents the lowest E_a and O_{vac}, highlighting the prevalent role of surface-active oxygen species (*i.e.* O_{ads}). Hence, two different stages occur: (1) Initially, at La/Mn atomic ratios above 0.7, the catalysts provide more cation vacancies (V_{La} and V_{Mn}) at the surface, compared with the stoichiometric $LaMnO_3$. Their presence likely induces the formation of unsaturated oxygen species and further facilitates the formation of surface-active O_{ads} species [31], as confirmed by XPS and TPR analyses. All mentioned factors would lead to a moderate improvement of the catalysts performance towards HCHO oxidation. (2) Further decreasing the La/Mn ratio from 0.7 promotes the formation of Mn_xO_y species at the surface of the perovskite. Their presence has a clear effect on the reactivity, by increasing the relative content of surface oxygen species [41], as shown by TPR. Moreover, it has been reported that MnO_x species are able to mineralize few ppm of HCHO from 25 °C under 25-30% of relative humidity over long periods [53]. In particular, V_{Mn} cationic vacancy is considered to enhance the lattice oxygen reactivity

and mobility, and lower the formation energy of oxygen vacancies. Besides, the decrease of Mn(AOS) involves the generation of oxygen vacancies to some degree. Active lattice oxygens are expected to play a major role in HCHO oxidation. It should be noted that the activity is well-correlated to the low-temperature reducibility of the catalysts. This result implies that surface oxygen species in La-deficient samples, which are the most reducible, have a predominant contribution over the global oxidation activity. In brief, the catalytic oxidation of HCHO herein may be considered as a function of the surface- and lattice-active oxygen species, and low-temperature reducibility of the catalysts (weaker Mn-O bonds).

3.6 Stability test and Moisture effect

Figure 9 illustrates the HCHO conversion into CO_2 and HCHO elimination under dry air over $La_{0.6}MnO_3$ at T_{50}. As seen, the catalyst maintains a relatively stable activity performance, however with an overtime decrease for both yields of about -20 % after 63 hours.

To investigate the possible changes of surface properties related to these lowered performances, $La_{0.6}MnO_3$ was again characterized after test. The XRD pattern (Figure S12a) of the spent catalyst appears unchanged. However, the TPR profile as displayed in Figure S12b reveals a lower consumption of H_2 below 600 °C (2.22 mmol/g) than the as-made $La_{0.6}MnO_3$ (2.81 mmol/g), implying that Mn species with lower valence state are present in the spent catalysts. Moreover, the onset temperature of reduction is shifted towards a higher temperature (225 °C instead of 147 °C), implying that less surface adsorbed oxygen species are present. Additionally, a shoulder (marked as red star in Figure S12b) can be clearly observed at 465 °C. O_2-TPD profile (Figure S9) also shows a lower oxygen desorption peak in the spent catalyst. All H_2-TPR and O_2-TPD data suggest that the $La_{0.6}MnO_3$ catalyst reducibility is decreased after the catalytic test,

in line with a decline of its overtime catalytic activity. Similarly, a slight change of the surface AOS (Mn) from 3.33 to 3.24, can be observed by XPS in the Mn 3s region (Figure S13a), which is in good agreement with TPR hydrogen consumed evolution.

XPS spectra in the O1s region of the catalyst before and after reaction are shown in Figure S13b. After test, the relative content of lattice oxygen species (O_{latt}) decreased considerably, from 67.7 % to 55.1 %. This correlates with the observed global manganese reduction following O_{latt} consumption during HCHO oxidation. Besides, the relative contents of surface adsorbed oxygen species (O_{ads}) and surface water (O_w) increased, which is attributed to the formation of surface oxygen species (mainly surface -OH groups) and the adsorption of water formed during the decomposition of formate species ($HCOO^-_{ads}$) [54], an intermediate product of HCHO oxidation. This phenomenon would counterbalance up to some point the decrease of O_{ads} and O_{latt}, and thus sustain the activity over long periods.

Of note, and as reported before [5,32], a contribution named C_F emerged around 288.6 eV on the XPS spectrum in the C 1s region of the spent catalyst, which refers to the presence of formate and HCHO species on the surface. Its low intensity implies that these species transform or desorb faster over $La_{0.6}MnO_3$. This observation was confirmed by the ToF-SIMS spectra displayed in Figure S14, showing four times more fragments attributed to HCHO intermediates (based on CO_3^-) on the surface of $LaMnO_3$ than on the surface of $La_{0.6}MnO_3$.

Mild temperature catalytic oxidation is known to be greatly affected by moisture, the presence of which is unavoidable in most practical applications. We recently reported that a controlled moisture is not only beneficial to the desorption of carbonate adsorbed on the active sites, but it also facilitates the regeneration of surface -OH groups, greatly enhancing the activity of $La_{1-x}A'_xMnO_3$ catalysts [5]. Here the catalytic

activity of $La_{0.6}MnO_3$ under humid conditions (relative humidity (RH) = 46 % at room temperature) was evaluated and the results are shown in Figure 10. As can be seen, the presence of H_2O greatly improves the overtime catalytic activity of $La_{0.6}MnO_3$, with constant HCHO elimination and conversion yields up to 63 hours at T_{50}.

In a typical HCHO oxidation process, HCHO is first adsorbed on the catalyst surface, and then oxidized by surface active oxygen species (O^*: O_2^-, O^-, -OH) into formate species (Eqs. 3 and 4) [30,31]. Further oxidation of formate by O^* generates carbonate species (Eq. 5) and finally CO_2 (Eqs. 6 and 7) [30,55]. The consumed O^* can be regenerated by the complex migration from surface O_{latt} to oxygen vacancies with the continuous dissociation of molecular oxygen, while the transfer from gas-phase oxygen to surface O_{latt} can be completed *via* the oxygen transfer mechanism (Eqs. 8-10) [30]. Additionally, surface -OH groups can be also replenished *via* the reaction between O^* and water (Eq. 11). Thus, in the presence of moisture, the catalytic cycle is looped.

$$HCHO_{ads} + 2O^* \rightarrow HCOO^-_{ads} + \text{-OH} \quad (3)$$

$$HCHO_{ads} + O^* \rightarrow HCOO^-_{ads} + H^+ \quad (4)$$

$$HCOO^-_{ads} + O^* \rightarrow HCO_3^-{}_{ads} \quad (5)$$

$$HCO_3^-{}_{ads} + OH^- \rightarrow CO_3^{2-}{}_{ads} + H_2O \quad (6)$$

$$HCO_3^-{}_{ads} + H^+ \rightarrow H_2CO_3{}_{ads} \rightarrow CO_2 + H_2O \quad (7)$$

$$Mn^{4+}\text{-}(O^{2-})\text{-}Mn^{4+} \rightarrow Mn^{3+}\text{-}(\square)\text{-}Mn^{3+} + O^*/O_2 \quad (8)$$

$$Mn^{4+}\text{-}(O^{2-})\text{-}Mn^{4+} + O^* + HCHO \rightarrow Mn^{3+}\text{-}(\square)\text{-}Mn^{3+} + CO_2 + H_2O \quad (9)$$

$$Mn^{3+}\text{-}(\square)\text{-}Mn^{3+} + O_2 \rightarrow Mn^{4+}\text{-}(O^{2-})\text{-}Mn^{4+} + O^* \quad (10)$$

$$H_2O + O^* \rightarrow 2\ \text{-OH} \quad (11)$$

"□" represents oxygen vacancies.

Under the studied conditions and as reported in the case of manganese oxide [30],

moisture regenerates the surface hydroxyl groups and further limits the accumulation of formate or carbonate species on the surface of $La_{0.6}MnO_3$. In turns, it facilitates the activation of H_2O and chemisorbed oxygen, therefore resulting in stable long-term oxidation performance.

4. Conclusions

This work correlates the La-deficiency level of $La_{1-x}MnO_3$ perovskite-based materials and their catalytic activity for HCHO oxidation. Hence the material with the lowest La/Mn ratio, $La_{0.6}MnO_3$, presented the highest activity with a T50 of 128 °C (against 145 °C for $LaMnO_3$) along with an apparent activation energy (E_a) of 43.7 kJ/mol (against 96.4 kJ/mol for $LaMnO_3$). This improvement in activity was attributed to more reducible and active surface adsorbed oxygen species. Especially, highly reducible Mn_xO_y species are formed besides the main perovskite phase when the La/Mn atomic ratio was below 0.8, and the resulting materials displayed improved HCHO oxidation performances owing to the enhanced reactivity and mobility of lattice oxygens, as well as the low-temperature reducibility of the metal oxide species. Moreover, under the presence of moisture, the catalytic performance of $La_{0.6}MnO_3$ was completely retained (100 % HCHO elimination and 50 % HCHO conversion into CO_2) for up to 63 hours at T50 which is an important characteristic in view of practical applications. Therefore, these results contribute to the development of low-cost and high-efficiency materials for indoor pollution control. Efforts should now be directed towards lowering its temperature of catalytic activity, meaning providing active oxygens at lower temperatures, for practical use.

Acknowledgments

The CNRS, the Chevreul Institute (FR 2638), the Ministère de l'Enseignement Supérieur et de la Recherche, the Région Hauts-de-France, the FEDER, the National

Natural Science Foundation of China (Grant No. 22006034) and the Hubei Provincial Natural Science Foundation of China (Grant No. 2020CFB485) are acknowledged for supporting this work. Yin Xu acknowledges the China Scholarship Council (No. 201606270079) for the financial support for the PhD program. The authors acknowledge Dr. Pardis Simon (UCCS) for XPS, Dr. Nicolas Nuns (IMEC) for ToF-SIMS, and Mr Olivier Gardoll (UCCS) for O_2-TPD characterizations.

References

[1] J. Hwang, R. R. Rao, L. Giordano, Y. Katayama, Y. Yu, Y. Shao-Horn, Perovskites in catalysis and electrocatalysis. Science 358 (2017) 751-756.

[2] S. Royer, D. Duprez, F. Can, X. Courtois, C.B. Dupeyrat, S. Laassiri, H. Alamdari, Perovskites as substitutes of noble metals for heterogeneous catalysis: dream or reality, Chem. Rev. 114 (2014) 10292-10368.

[3] H. Arandiyan, S. S. Mofarah, C. C. Sorrell, E. Doustkhah, B. Sajjadi, D. Hao, Y. Wang, H. Sun, B. Ni, M. Rezaei, Z. P. Shao, T. Maschmeyer, Defect engineering of oxide perovskites for catalysis and energy storage: synthesis of chemistry and materials science. Chem. Soc. Rev. 50 (2021) 10116-10211.

[4] H. Najjar, H. Batis, Development of Mn-based perovskite materials: Chemical structure and applications. Catal. Rev. 58 (2016) 371-438.

[5] Y. Xu, J. Dhainaut, J.-P. Dacquin, A.-S. Mamede, M. Marinova, J.-F. Lamonier, H. Vezin, H. Zhang, S. Royer, $La_{1-x}(Sr, Na, K)_xMnO_3$ perovskites for HCHO oxidation: The role of oxygen species on the catalytic mechanism, Appl. Catal. B 287 (2021) 119955.

[6] X. Yang, T. Wei, B. Chi, J. Pu, J. Li, Lanthanum manganite-based perovskite as a catalyst for co-production of ethylene and hydrogen by ethane dehydrogenation. J. Catal. 377 (2019) 629-637.

[7] K. Wang, C. Han, Z. Shao, J. Qiu, S. Wang, S. Liu, Perovskite oxide catalysts for advanced oxidation reactions. Adv. Fun. Mater. 31 (2021) 2102089.

[8] S. Royer, B. Levasseur, H. Alamdari, J. Barbier Jr, D. Duprez, S. Kaliaguine, Mechanism of stearic acid oxidation over nanocrystalline $La_{1-x}A'_xBO_3$ (A′= Sr, Ce; B= Co, Mn): The role of oxygen mobility, Appl. Catal. B 80 (2008) 51-61.

[9] H. Wang, J. Zhang, X. Hang, X. Zhang, J. Xie, B. Pan, Y. Xie, Half-Metallicity in

Single-layered manganese dioxide nanosheets by defect engineering, Angew. Chem. Int. Edit. 127 (2015) 1211-1215.

[10] K.D. Kwon, K. Refson, G. Sposito, Defect-induced photoconductivity in layered manganese oxides: A density functional theory study, Phys. Rev. lett. 100 (2008) 146601.

[11] X. Xu, Y. Pan, L. Ge, Y.B. Chen, X. Mao, D.Q. Guan, M.R. Li, Y.J. Zhong, Z.W. Hu, V.K. Peterson, M. Saunders, C.T. Chen, H.J. Zhang, R. Ran, A. Du, H. Wang, S.P. Jiang, W. Zhou, Z.P. Shao, High-performance perovskite composite electrocatalysts enabled by controllable interface engineering, Small 17 (2021) 2101573.

[12] X. Xu, W. Wang, W. Zhou, Z.P. Shao, Recent advances in novel nanostructuring methods of perovskite electrocatalysts for energy-related applications. Small Methods 2 (2018) 1800071.

[13] J. He, X. Xu, M. Li, S. Zhou, W. Zhou, Recent advances in perovskite oxides for non-enzymatic electrochemical sensors: A review, Anal. Chim. Acta, 1251 (2023) 341007.

[14] D. Chen, M. Qiao, Y.R. Lu, L. Hao, D. Liu, C.L. Dong, Y. Li, S. Wang, Preferential cation vacancies in perovskite hydroxide for the oxygen evolution reaction. Angew. Chem. Int. Edit. 57 (2018) 8691-8696.

[15] Y. Zhu, W. Zhou, J. Yu, Y. Chen, M. Liu, Z. Shao, Enhancing electrocatalytic activity of perovskite oxides by tuning cation deficiency for oxygen reduction and evolution reactions. Chem. Mater. 28 (2016) 1691-1697.

[16] Y. Qiu, R. Gao, W. Yang, L. Huang, Q. Mao, J. Yang, L. Sun, Z. Hu, X. Liu, Understanding the enhancement mechanism of A site-deficient La_xNiO_3 as an oxygen redox catalyst. Chem. Mater. 32 (2020) 1864-1875.

[17] J.A.M. Van Roosmalen, E.H.P. Cordfunke, R.B. Helmholdt, H.W. Zandbergen. The defect chemistry of $LaMnO_{3\pm\delta}$: 2. Structural aspects of $LaMnO_{3+\delta}$. J. Solid State Chem. 110 (1994) 100-105.

[18] J.A. Alonso, M.J. Martinez-Lope, M.T. Casais, J.L. MacManus-Driscoll, P.S. De Silva, L.F. Cohen, M.T. Fernandez-Diaz, Non-stoichiometry, structural defects and properties of $LaMnO_{3+\delta}$ with high δ values ($0.11 \leq \delta \leq 0.29$), J. Mater. Chem. 7 (1997) 2139-2144.

[19] G. Dezanneau, A. Sin, H. Roussel, M. Audier, H. Vincent, Magnetic properties related to structure and complete composition analyses of nanocrystalline $La_{1-x}Mn_{1-y}O_3$ powders, J. Solid State Chem. 173 (2003) 216-226.

[20] A.N. Ulyanov, H.J. Shin, D.S. Yang, S.V. Savilov, N.E. Pismenova, E.A. Goodilin, Hybridization of electronic states and magnetic properties of self-doped $La_{1-x}MnO_{3+\delta}$ ($0\leq x\leq 0.15$) perovskites: XANES study, J. Magn. Magn. Mater. 458 (2018) 134-136.

[21] J. Faye, A. Baylet, M. Trentesaux, S. Royer, F. Dumeignil, D. Duprez, S. Valange, J.M. Tatibouët, Influence of lanthanum stoichiometry in $La_{1-x}FeO_{3-\delta}$ perovskites on their structure and catalytic performance in CH_4 total oxidation. Appl. Catal. B 126 (2012) 134-143.

[22] J. Chen, M. Shen, X. Wang, G. Qi, J. Wang, W. Li, The influence of nonstoichiometry on $LaMnO_3$ perovskite for catalytic NO oxidation, Appl. Catal. B 134 (2013) 251-257.

[23] L. Fang, N. Liu, W. Liu, J. Mo, Z. Zhao, H. Kan, F. Deng., C. Huang., B. Zhao., X. Zeng., Y. Sun., H. Qian., C. Sun., J. Guo., X. Zheng., Y., Zhang, Indoor formaldehyde levels in residences, schools, and offices in China in the past 30 years: A systematic review. Indoor air, 32 (2022) e13141.

[24] ARC.IARC classifies formaldehyde as carcinogenic to humans; press release no.153; International Agency for Research on Cancer: Lyon, 2004.

[25] J. Ye, Y. Yu, J. Fan, B. Cheng, J. Yu, W. Ho, Room-temperature formaldehyde catalytic decomposition. Environ. Sci. Nano 7 (2020) 3655-3709.

[26] K. Vellingiri, K. Vikrant, V. Kumar, K. H. Kim, Advances in thermocatalytic and photocatalytic techniques for the room/low temperature oxidative removal of formaldehyde in air. Chem. Eng. J. 399 (2020) 125759.

[27] S. Chen, S. Gueddida, M. Badawi, S. Lebègue, J.-M. Giraudon, J. Dhainaut, S. Royer, J.-F. Lamonier, Unravelling the critical role of silanol in Pt/SiO_2 for room temperature HCHO oxidation: An experimental and DFT study, Appl. Catal. B331 (2023) 122672.

[28] J. Ye, B. Zhu, B. Cheng, C. Jiang, S. Wageh, A. A. Al-Ghamdi, J. Yu, Synergy between platinum and gold nanoparticles in oxygen activation for enhanced room-temperature formaldehyde oxidation. Adv. Fun. Mater. 3 (2022) 2110423.

[29] J.H. Zhang, Y.B. Li, L. Wang, C.B. Zhang, H. He, Catalytic oxidation of formaldehyde over manganese oxides with different crystal structures, Catal. Sci. Technol. 5 (2015) 2305-2313.

[30] J.L. Wang, P.Y. Zhang, J.G. Li, C.J. Jiang, R. Yunus, J. Kim, Room-temperature oxidation of formaldehyde by layered manganese oxide: effect of water, Environ. Sci. Technol. 49 (2015) 12372-12379.

[31] J.L. Wang, J.G. Li, C.J. Jiang, P. Zhou, P.Y. Zhang, J.G. Yu, The effect of manganese vacancy in birnessite-type MnO_2 on room-temperature oxidation of formaldehyde in air, Appl. Catal. B 204 (2017) 147-155.

[32] S. Selvakumar, N. Nuns, M. Trentesaux, V.S. Batra, J.M. Giraudon, J.F. Lamonier, Reaction of formaldehyde over birnessite catalyst: A combined XPS and ToF-SIMS

study, Appl. Catal. B 223 (2018) 192-200.

[33] J. Ding, J. Liu, Y. Yang, L. Zhao, Y. Yu, Understanding A-site tuning effect on formaldehyde catalytic oxidation over La-Mn perovskite catalysts. J. Hazard. Mater. 422 (2022) 126931.

[34] Y. Xu, J. Dhainaut, G. Rochard, J. P. Dacquin, A. S. Mamede, J. M. Giraudon, J. F. Lamonier, H. Zhang, S. Royer, Hierarchical porous ε-MnO_2 from perovskite precursor: Application to the formaldehyde total oxidation. Chem. Eng. J. 388 (2020) 124146.

[35] V. Markovich, I. Fita, D. Mogilyansky, A. Wisniewski, R. Puzniak, L. Titelman, L. Vradman, G. Gorodetsky, Magnetic properties of nanocrystalline $La_{1-x}MnO_{3+\delta}$ manganites: size effects, J. Phys. Condens. Mat. 19 (2007) 346210.

[36] A.R. Shelke, N.G. Deshpande, Influence of the calcination temperature on the combustion synthesized perovskite $LaMnO_3$ compound, J. Nano-Electron. Phys. 7 (2015) 03009-1.

[37] Z. Gao, H. Wang, H. Ma, Z. Li, Preparation and characterization of the non-stoichiometric La-Mn perovskites. J. Alloy. Compd. 646 (2015) 73-79.

[38] Y. Yang, J. Huang, S. Wang, S. Deng, B. Wang, G. Yu, Catalytic removal of gaseous unintentional POPs on manganese oxide octahedral molecular sieves, Appl. Catal. B 142-143 (2013) 567-568.

[39] J.G. Deng, L. Zhang, H.X. Dai, H. He, C.T. Au, Strontium-doped lanthanum cobaltite and manganite: highly active catalysts for toluene complete oxidation, Ind. Eng. Chem. Res. 47 (2008) 8175-8183.

[40] C.B. Zhang, F.D. Liu, Y.P. Zhai, H. Ariga, N. Yi, Y.C. Liu, K. Asakura, Alkali-metal-promoted Pt/TiO_2 opens a more efficient pathway to formaldehyde oxidation at ambient temperatures, Angew. Chem. Int. Ed. 51 (2012) 9628-9632.

[41] V.P. Santos, M.F.R. Pereira, J.J.M. Órfão, J.L. Figueiredo, The role of lattice oxygen on the activity of manganese oxides towards the oxidation of volatile organic compounds, Appl. Catal. B 99 (2010) 353-363.

[42] E. Granado, J. A. Sanjurjo, C. Rettori, J. J., Neumeier, S. B. Oseroff, Order-disorder in the Jahn-Teller transition of $LaMnO_3$: A Raman scattering study. Physical Review B, 62 (2000) 11304.

[43] F. Teng, W. Han, S. Liang, B. Gaugeu, R. Zong, Y. Zhu, Catalytic behavior of hydrothermally synthesized $La_{0.5}Sr_{0.5}MnO_3$ single-crystal cubes in the oxidation of CO and CH_4. J. Catal. 250 (2007) 1-11.

[44] Y. Wang, Y. Zheng, Y. Wang, H. Wang, X. Zhu, Y. Wei, Y. Wang, L. Jiang, Z. Yang, K. Li, Evaluation of Fe substitution in perovskite $LaMnO_3$ for the production of high purity syngas and hydrogen. J. Power Sources, 449 (2020) 227505.

[45] D. Yu, W. Xingyi, L. Dao, D. Qiguang, Catalytic combustion of chlorobenzene over Mn-Ce-La-O mixed oxide catalysts. J. Hazard. Mater. 188 (2011) 132-139.

[46] N. Huang, Z. Qu, C. Dong, Y. Qin, X. Duan, Superior performance of α@ β-MnO_2 for the toluene oxidation: Active interface and oxygen vacancy. Appl. Catal. A 560 (2018) 195-205.

[47] Y. Wang, H. P. Cheng, Oxygen reduction activity on perovskite oxide surfaces: a comparative first-principles study of $LaMnO_3$, $LaFeO_3$, and $LaCrO_3$. J. Phys. Chem. C 117 (2013) 2106-2112.

[48] D. Du, R. Zheng, M. He, C. Zhao, B. Zhou, R. Li, C. Shu, A-site cationic defects induced electronic structure regulation of $LaMnO_3$ perovskite boosts oxygen electrode reactions in aprotic lithium–oxygen batteries. Energy Storage Mater. 43 (2021) 293-304.

[49] F. Abild-Pedersen, J. Greeley, F. Studt, J. Rossmeisl, T. R. Munter, P. G. Moses, E.

Skúlason, T. Bligaard, J. K. Nørskov, Scaling properties of adsorption energies for hydrogen-containing molecules on transition-metal surfaces. Phys. Rev. Lett. 99 (2007) 016105.

[50] E.D. Stobbe, B.A. De Boer, J.W. Geus, The reduction and oxidation behaviour of manganese oxides, Catal. Today 47 (1999) 161-167.

[51] Y. Chen, Z. Huang, M. Zhou, P. Hu, C. Du, L. Kong, J.M. Chen, X.F. Tang, The active sites of supported silver particle catalysts in formaldehyde oxidation, Chem. Commun. 52 (2016) 9996-9999.

[52] J. Chen, D. Yan, Z. Xu, X. Chen, X. Chen, W.J. Xu, H.P. Jia, J. Chen, A novel redox precipitation to synthesize Au-doped α-MnO_2 with High Dispersion toward low-temperature oxidation of formaldehyde, Environ. Sci. Technol. 52 (2018) 4728-4737.

[53] J. Zheng, W. Zhao, L. Song, H. Wang, H. Yan, G. Chen, C. Han, J. Zhang, Advances of manganese-oxides-based catalysts for indoor formaldehyde removal. Green Energy Environ. 8 (2023) 626-653.

[54] J. Quiroz, J.M. Giraudon, A. Gervasini, C. Dujardin, C. Lancelot, M. Trentesaux, J.F. Lamonier, Total oxidation of formaldehyde over MnO_x-CeO_2 catalysts: The effect of acid treatment, ACS Catal. 5 (2015) 2260-2269.

[55] C. Wang, Y. Li, L. Zheng, C. Zhang, Y. Wang, W. Shan, F. Liu, H. He, A nonoxide catalyst system study: Alkali metal-promoted Pt/AC catalyst for formaldehyde oxidation at ambient temperature. ACS Catal. 11 (2020) 456-465.

Figure Captions

Figure 1 EDS mapping of La, Mn, and O on the surface of $La_{0.6}MnO_3$.

Figure 2 XPS spectra of (a) Mn 3s and (b) O 1s of the $La_{1-x}MnO_3$ series (x = 0 to 0.4).

Figure 3 EPR spectra of the $La_{1-x}MnO_3$ series (x = 0 to 0.4). Inset: linear relationship between the amount of oxygen vacancies and the La-deficiency.

Figure 4 Side view of perovskite (001) surfaces: (a) $LaMnO_3$, (b) $La_{1-x}MnO_3$, (c) $LaMnO_{3-y}$; (d) $La_{1-x}MnO_{3-y}$.

Figure 5 Calculated (a, b) *d*-band centers of Mn and (c, d) *p*-band centers of O on perovskite (001) surfaces: (a, c) $LaMnO_3$ and (b, d) $La_{1-x}MnO_3$.

Figure 6 H_2-TPR profiles of the $La_{1-x}MnO_3$ series (x = 0 to 0.4).

Figure 7 XRD patterns of $La_{0.6}MnO_3$ during *in-situ* temperature-programmed reduction up to 800 °C.

Figure 8 HCHO catalytic oxidation over the $La_{1-x}MnO_3$ series (x = 0 to 0.4): (a) HCHO conversion into CO_2 and (b) corresponding Arrhenius plots.

Figure 9 Overtime HCHO conversion over $La_{0.6}MnO_3$ under dry conditions at T50 = 128 °C.

Figure 10 Overtime HCHO conversion over $La_{0.6}MnO_3$ under humid conditions at T50 = 128 °C.

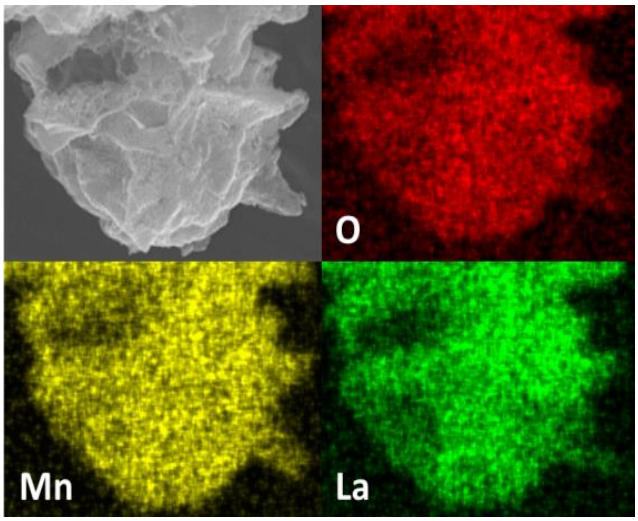

Figure 1

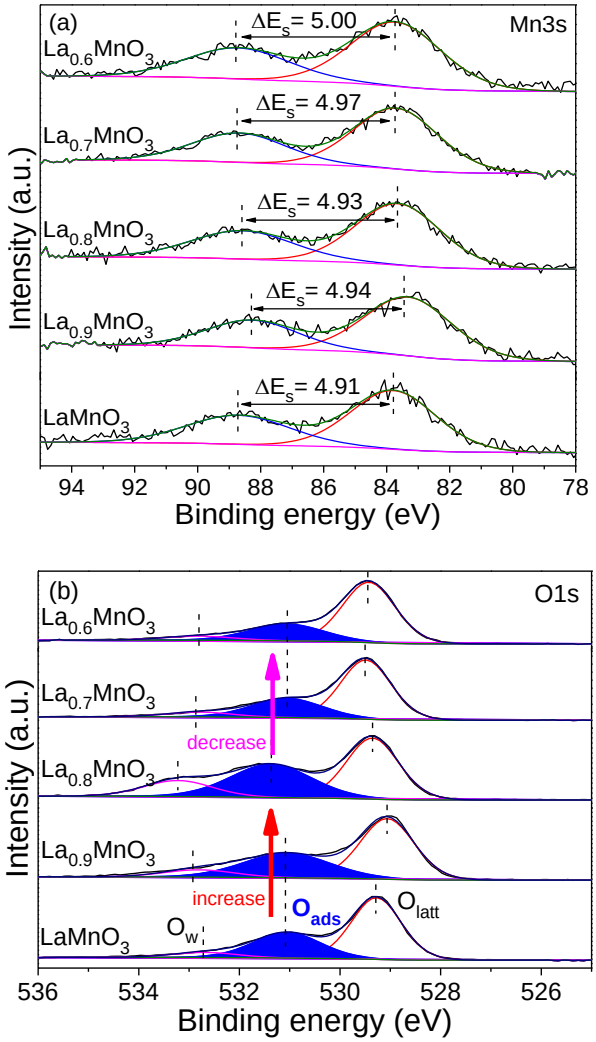
(a)
Mn3s
ΔE_s= 5.00
La0.6MnO3
ΔE_s= 4.97
La0.7MnO3
ΔE_s= 4.93
La0.8MnO3
ΔE_s= 4.94
La0.9MnO3
ΔE_s= 4.91
LaMnO3
Intensity (a.u.)
94 92 90 88 86 84 82 80 78
Binding energy (eV)
(b)
O1s
La0.6MnO3
La0.7MnO3
decrease
La0.8MnO3
La0.9MnO3
increase
O_ads
O_latt
LaMnO3
O_w
Intensity (a.u.)
536 534 532 530 528 526
Binding energy (eV)

Figure 2

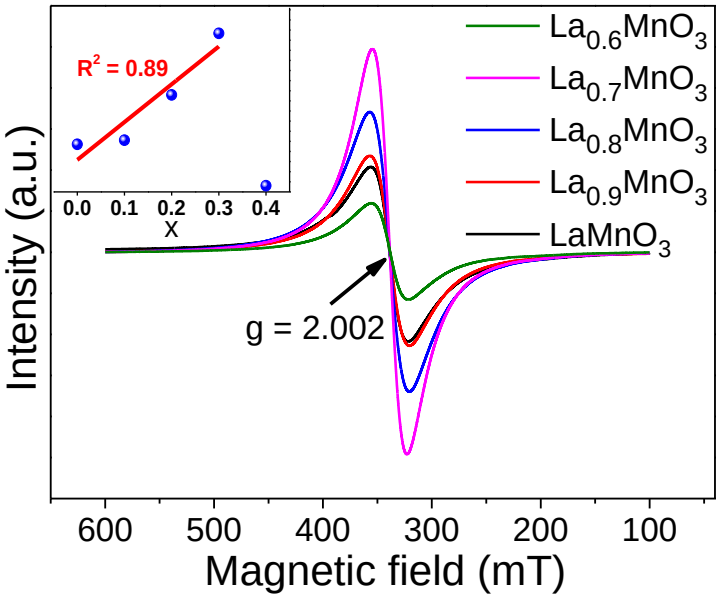
Intensity (a.u.)
Magnetic field (mT)
600
500
400
300
200
100
La0.6MnO3
La0.7MnO3
La0.8MnO3
La0.9MnO3
LaMnO3
g = 2.002
R2 = 0.89
0.0
0.1
0.2
0.3
0.4
X

Figure 3

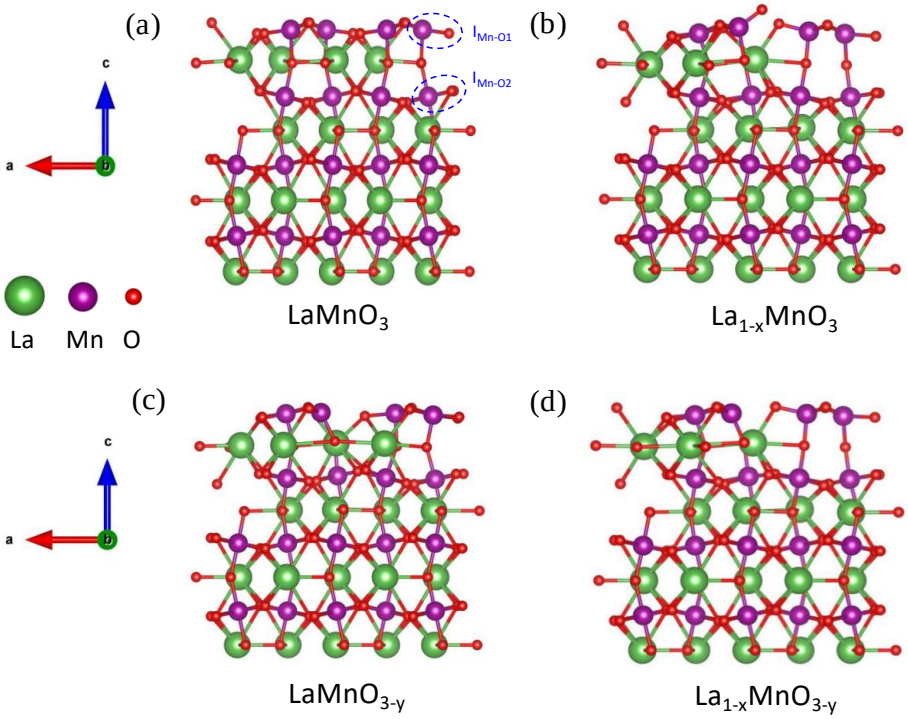
(a)
(b)
(c)
(d)
c
a
b
La
Mn
O
l_{Mn-O1}
l_{Mn-O2}
$LaMnO_3$
$La_{1-x}MnO_3$
$LaMnO_{3-y}$
$La_{1-x}MnO_{3-y}$

Figure 4

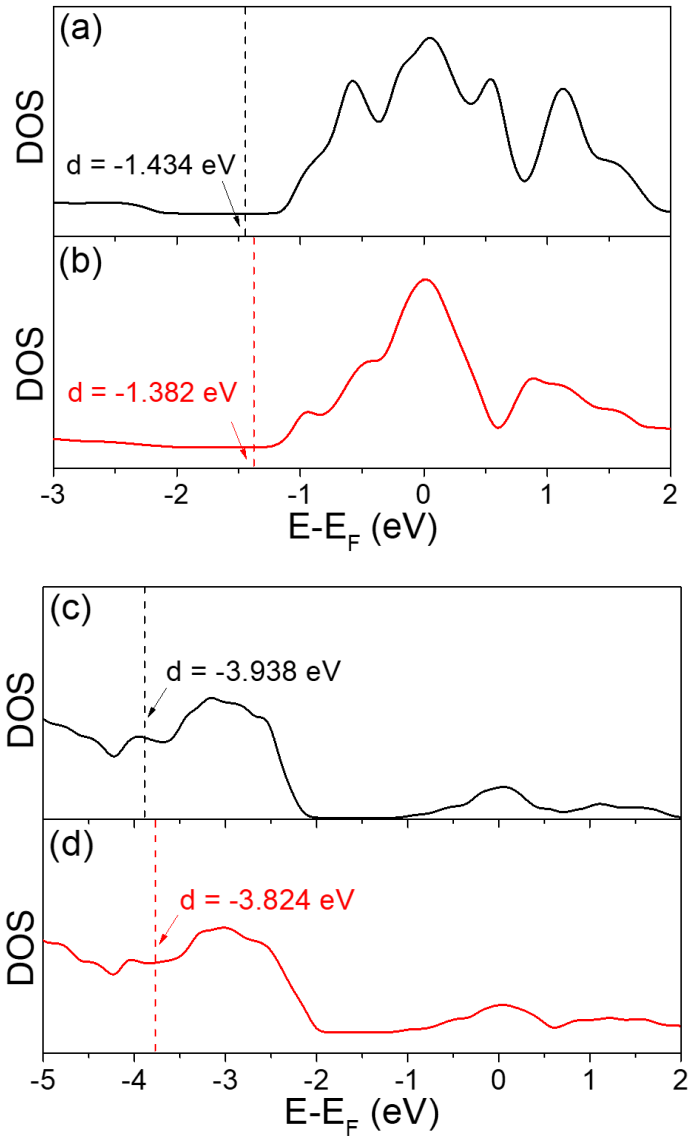
(a)
DOS
d = -1.434 eV
(b)
DOS
d = -1.382 eV
-3
-2
-1
0
1
2
E-E$_F$ (eV)
(c)
DOS
d = -3.938 eV
(d)
DOS
d = -3.824 eV
-5
-4
-3
-2
-1
0
1
2
E-E$_F$ (eV)

Figure 5

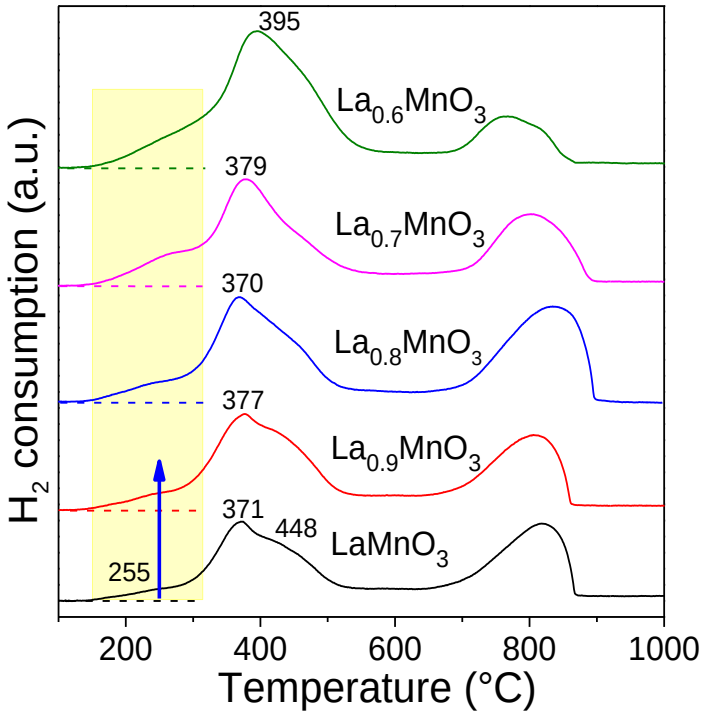
395
La0.6MnO3
379
La0.7MnO3
370
La0.8MnO3
377
La0.9MnO3
371
448
LaMnO3
255
H2 consumption (a.u.)
200
400
600
800
1000
Temperature (°C)

Figure 6

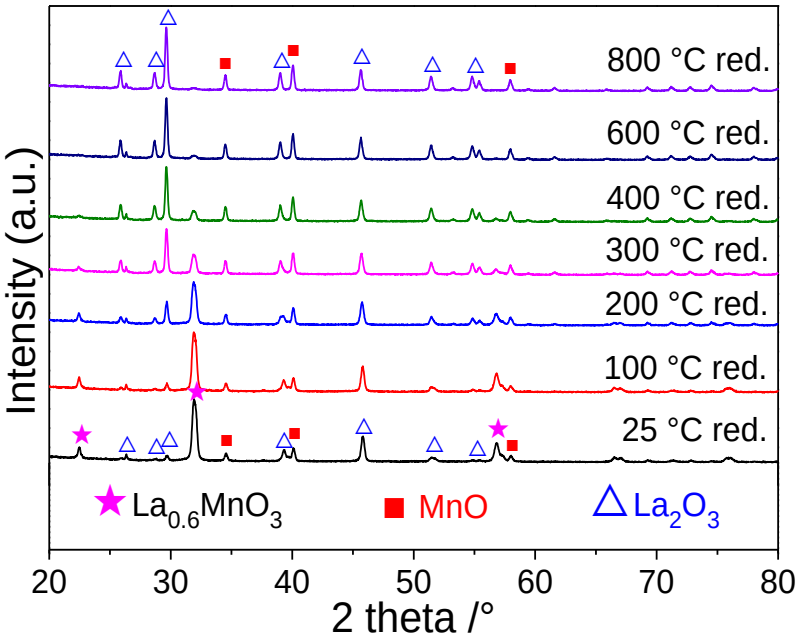
800 °C red.
600 °C red.
400 °C red.
300 °C red.
200 °C red.
100 °C red.
25 °C red.
Intensity (a.u.)
La0.6MnO3
MnO
La2O3
20
30
40
50
60
70
80
2 theta /°

Figure 7

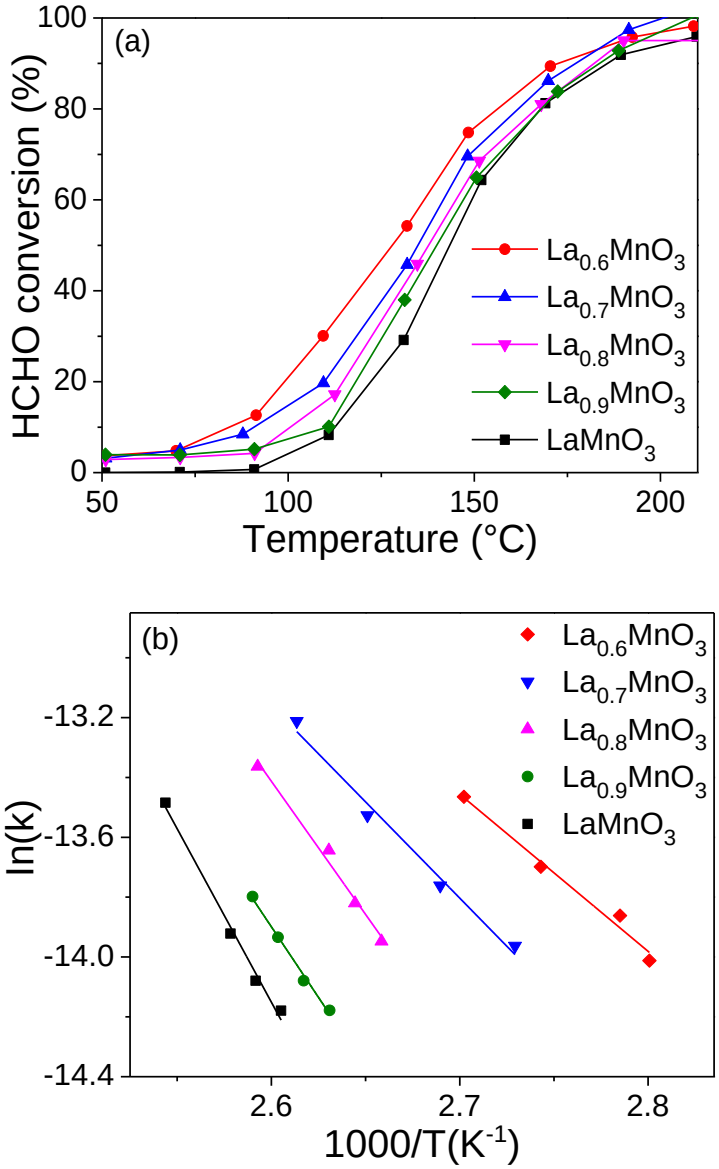
(a)
HCHO conversion (%)
Temperature (°C)
La0.6MnO3
La0.7MnO3
La0.8MnO3
La0.9MnO3
LaMnO3
(b)
ln(k)
1000/T(K-1)

Figure 8

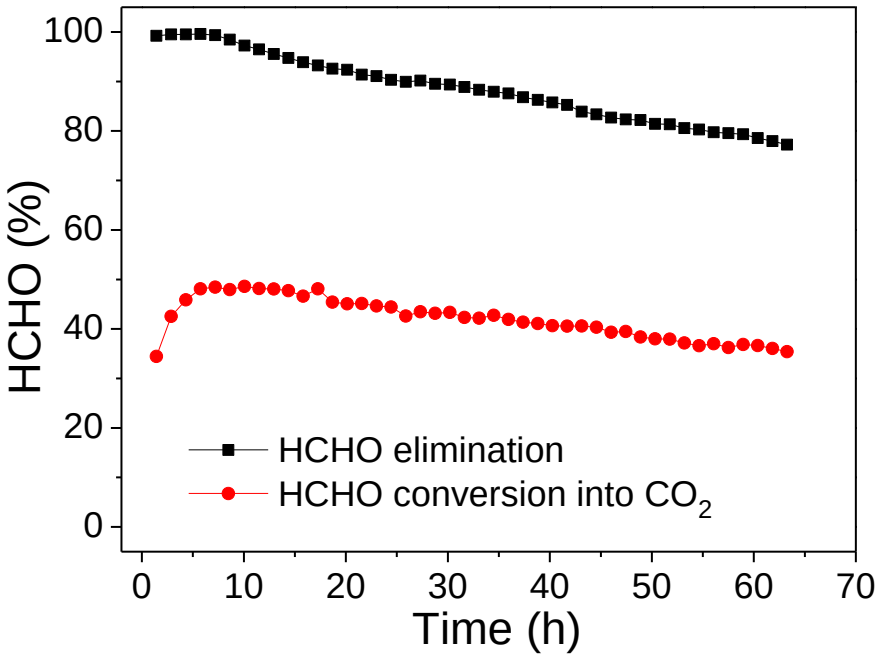
100
80
60
40
20
0
HCHO (%)
0
10
20
30
40
50
60
70
Time (h)
HCHO elimination
HCHO conversion into CO2

Figure 9

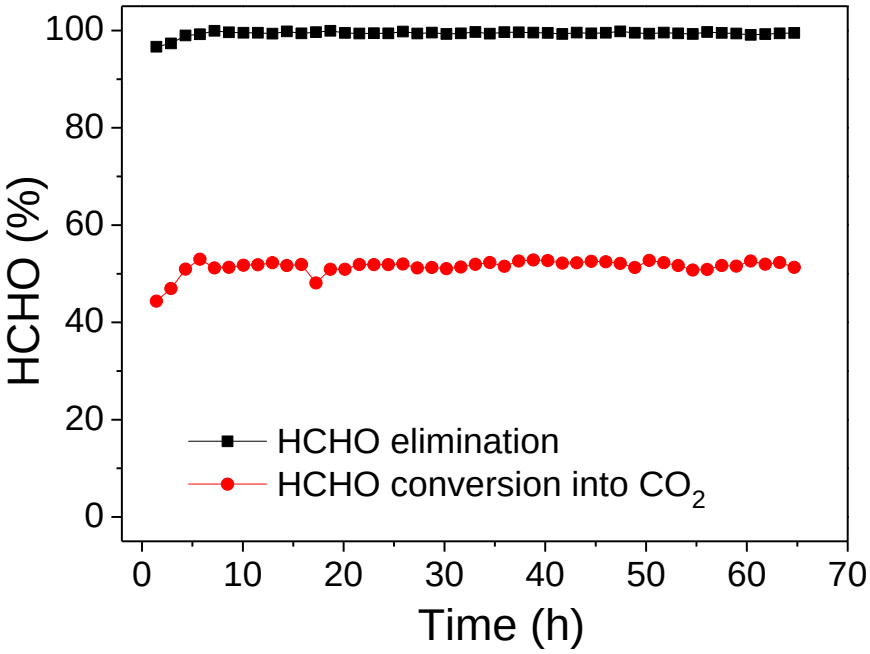
100
80
60
40
20
0
HCHO (%)
0
10
20
30
40
50
60
70
Time (h)
HCHO elimination
HCHO conversion into CO2

Figure 10

Table 1

Textural and structural properties of the $La_{1-x}MnO_3$ series (x = 0 to 0.4).

Samples	Crystalline phases[a]	S_{BET} (m^2/g)	d (nm)
$LaMnO_3$	LMO	18	26
$La_{0.9}MnO_3$	LMO	22	24
$La_{0.8}MnO_3$	LMO	20	23
$La_{0.7}MnO_3$	LMO/Mn_xO_y	24	21
$La_{0.6}MnO_3$	LMO/Mn_xO_y	22	19

[a] As identified by X-ray diffraction.

Table 2

Relative surface abundances of the elements constituting the $La_{1-x}MnO_3$ series (x = 0 to 0.4).

Samples	La/Mn		Mn/O	La/O	AOS (Mn)	O_{latt}/O_{tot}	O_{ads}/O_{tot}
	ICP	XPS					
$LaMnO_3$	1.01	1.12	0.95:3	1.06:3	3.42	0.59	0.34
$La_{0.9}MnO_3$	0.88	0.87	0.83:3	0.73:3	3.40	0.56	0.35
$La_{0.8}MnO_3$	0.84	0.73	0.71:3	0.52:3	3.41	0.46	0.39
$La_{0.7}MnO_3$	0.69	0.49	1.14:3	0.56:3	3.36	0.64	0.29
$La_{0.6}MnO_3$	0.60	0.42	1.21:3	0.51:3	3.33	0.68	0.26

Table 3

H_2 consumption deduced from the H_2-TPR for the $La_{1-x}MnO_3$ series (x = 0 to 0.4).

Samples	T_{max} reduction peaks (°C)		H_2 consumption (mmol/g)		
	t1	t2	peak 1	peak 2	Total
$LaMnO_3$	371	818	1.52	1.14	2.66
$La_{0.9}MnO_3$	377	806	1.83	1.06	2.89
$La_{0.8}MnO_3$	370	830	1.71	1.34	3.05
$La_{0.7}MnO_3$	379	803	2.11	1.10	3.21
$La_{0.6}MnO_3$	395	766	2.81	0.58	3.39

Table 4

HCHO oxidation over the $La_{1-x}MnO_3$ series (x = 0 to 0.4) and Mn_3O_4.

Samples	HCHO conversion temperature (°C)		
	T10	T50	T90
$LaMnO_3$	114	145	183
$La_{0.9}MnO_3$	111	141	183
$La_{0.8}MnO_3$	103	137	183
$La_{0.7}MnO_3$	93	135	177
$La_{0.6}MnO_3$	84	128	171
Mn_3O_4	187	205	218